The Astrophysical Journal, 821:31 (15pp), 2016 April 10 doi:10.3847/0004-637X/821/1/31

MULTI-VIEWPOINT OBSERVATIONS OF A WIDELY DISTRIBUTED SOLAR ENERGETIC PARTICLE EVENT: THE ROLE OF EUV WAVES AND WHITE-LIGHT SHOCK SIGNATURES

A. Kouloumvakos[1], S. Patsourakos[1], A. Nindos[1], A. Vourlidas[2], A. Anastasiadis[3], A. Hillaris[4], and I. Sandberg[3]
[1] Section of Astrogeophysics, Department of Physics, University of Ioannina, 45110 Ioannina, Greece
[2] The Johns Hopkins University Applied Physics Laboratory, Laurel, MD 20723, USA
[3] Institute for Astronomy, Astrophysics, Space Applications and Remote Sensing, National Observatory of Athens, 15236 Penteli, Greece
[4] Section of Astrophysics, Astronomy and Mechanics, Department of Physics, National and Kapodistrian University of Athens, 15783 Athens, Greece
Received 2015 June 22; accepted 2016 February 20; published 2016 April 5

ABSTRACT

On 2012 March 7, two large eruptive events occurred in the same active region within 1 hr from each other. Each consisted of an X-class flare, a coronal mass ejection (CME), an extreme-ultraviolet (EUV) wave, and a shock wave. The eruptions gave rise to a major solar energetic particle (SEP) event observed at widely separated (~120°) points in the heliosphere. From multi-viewpoint energetic proton recordings we determine the proton release times at *STEREO B* and *A* (*STB*, *STA*) and the first Lagrange point (L1) of the Sun–Earth system. Using EUV and white-light data, we determine the evolution of the EUV waves in the low corona and reconstruct the global structure and kinematics of the first CME's shock, respectively. We compare the energetic proton release time at each spacecraft with the EUV waves' arrival times at the magnetically connected regions and the timing and location of the CME shock. We find that the first flare/CME is responsible for the SEP event at all three locations. The proton release at *STB* is consistent with arrival of the EUV wave and CME shock at the *STB* footpoint. The proton release time at L1 was significantly delayed compared to *STB*. Three-dimensional modeling of the CME shock shows that the particle release at L1 is consistent with the timing and location of the shock's western flank. This indicates that at L1 the proton release did not occur in low corona but farther away from the Sun. However, the extent of the CME shock fails to explain the SEP event observed at *STA*. A transport process or a significantly distorted interplanetary magnetic field may be responsible.

Key words: Sun: corona – Sun: coronal mass ejections (CMEs) – Sun: flares – Sun: particle emission

Supporting material: animations

1. INTRODUCTION

Flares and coronal mass ejection (CME)-driven shocks can accelerate electrons and ions to high energies. These transient enhancements of particle levels are called solar energetic particle (SEP) events. The events are classified into two broad classes of impulsive and gradual events based on their rate of intensity rise and duration (e.g., Cane et al. 1986; Kallenrode et al. 1993; Reames 1999, 2013). The two SEP classes generally differ in the properties of their associated soft X-ray (SXR) flares, correlation with radio bursts, the presence or absence of a CME, their abundances, and charge states. Many gradual events spread widely in longitude as early multipoint observations from the *Helios*, *IMP8*, and *ISEE*-3 spacecraft have established. Interplanetary shocks were obvious candidates for the SEP spread since they are large-scale accelerators that can inject particles along wide longitudinal directions (e.g., Cane et al. 1988; Kallenrode et al. 1993). SEP events are associated with both coronal and interplanetary (IP) shocks (e.g., Krucker et al. 1999; Cliver et al. 2004; Rouillard et al. 2012). Since CMEs are the drivers of these shocks, CMEs have become major players in longitudinal particle transport (Reames 2013).

Examining the role of shocks in the longitudinal extent of SEPs generally involves relating the SEP intensities (at various locations/times) to the CME shock properties, mainly speed, direction, and size. Since the particle's intensities start rising when the CME is close to the Sun, remote observations of shocks are of paramount importance. Currently, we can observe CME-driven shocks in three regimes: radio, white light (WL), and extreme-ultraviolet (EUV). Frequency-drifting emissions (so-called type IIs) are the oldest method of detecting shocks remotely (Wild 1950) but can provide the shock speed under some assumption about the background electron density gradient. Occasionally, type II emission is captured by radio imaging instruments that provide some information on the general location of the shock albeit at very low spatial resolutions (~arcminutes). However, radio imaging is only possible at meter or shorter wavelengths, and hence it is restricted to a few solar radii from the solar surface. WL coronagraphs can image CME-driven shocks directly and provide some basic shock parameters, such as speed, direction, and density compression ratio (see Vourlidas & Bemporad 2012, for a review). Additionally, low coronal shocks can indirectly be inferred from EUV waves, i.e., large-scale propagating intensity fronts observed in the EUV, given that they are closely related to type II coronal and IP radio bursts (e.g., Klassen et al. 1999; Kouloumvakos et al. 2014; Nitta et al. 2014). EUV waves probe the inner corona and may be driven by the early CME expansion (e.g., Patsourakos & Vourlidas 2012; Nitta et al. 2013, and references therein). However, the WL and EUV observations provide only limited three-dimensional (3D) information on the shock when they are obtained from a single viewpoint, as was the case during the *Solar and Heliospheric Observatory* (*SOHO*) mission (Domingo et al. 1995).

The launch of the *Solar TErrestrial RElations Observatories* (*STEREO*; Kaiser et al. 2008) mission in 2006 marked a new era in the study of SEP events and their sources. The multiple vantage point remote-sensing and in situ *STEREO* observations have significantly improved our understanding of the SEP

events' acceleration and release in the heliosphere and their longitudinal extent (e.g., Rouillard et al. 2012; Wiedenbeck et al. 2013). Recent studies have suggested a scenario where the energetic particle release time is coincident to the arrival of the EUV wave to regions magnetically connected to the observer. From the analysis of the 2011 March 21 SEP event Rouillard et al. (2012) showed an association between the longitudinal extent of the perturbed corona, in both EUV and WL, and the longitudinal extent of the associated SEP event. Park et al. (2013) reached a similar conclusion based on a sample of 12 SEP events. Miteva et al. (2014) showed a similar connection between the *extrapolated* arrival times of EUV waves and energetic proton release times for a set of 28 eastern hemisphere events.

Other studies, on the other hand, suggest a weak or even no connection between EUV expansion and particle release. These studies suggest that the longitudinal spread of SEP events is due to the shock expansion at higher altitudes than those traced by EUV waves. For the event of 2011 November 3, Prise et al. (2013) studied the CME and EUV wave evolution without being able to discriminate the CME and CME-driven shock and showed that the particle release time at both *STEREO* spacecraft was *correlated* with the CME expansion time to well-connected magnetic field lines at each spacecraft. For the same event, Gómez-Herrero et al. (2015) showed that cross-field IP diffusion did not play a major role and supported a rapid particle longitudinal spread before the CME reached a heliocentric height of six solar radii. Lario et al. (2014), using a 3D analysis of the EUV wave and CME shock of the 2013 April 11 event, demonstrated that the angular extent of the EUV wave did not trace the SEP release time. They proposed that the CME-driven shock in the outer corona was the most likely source of the observed SEP event.

Hence, the relative role of EUV waves in the energetic particle release across wide longitudes is still under debate. Furthermore, most studies have investigated the 3D connection between shock extent and particle release either close to the Sun only or not at all. Finally, there has not been a study of SEPs associated with multiple CME events where magnetic connectivity is more difficult to establish.

In this paper, we attempt to address all three issues using multi-viewpoint WL and EUV imaging and in situ measurements of a major SEP event on 2012 March 7–8. It was one of the strongest proton events of 2012 and was detected by three spacecraft across at least 120° of longitude. The SEP event was associated with complex solar activity consisting of a pair of powerful flares, EUV waves, and CMEs in very close temporal proximity (within 1 hr of each other). The CMEs were very fast ($\sim$2000 km s^{-1}) and hence capable of driving shocks and accelerating SEPs, and one of them was Earth directed. We employ forward modeling to derive CME and shock direction and extent in 3D in order to address the following questions:

1. Which of the two events caused the rise of energetic protons at each observing point?
2. What is the contribution of the flares and CMEs in the particle acceleration?
3. What is the connection between the observed EUV waves and particle release at *STEREO-B*/*A* and L1?
4. What is the role of the shock's *nose* versus its *flanks* in energetic particle release at *STEREO-B*/*A* and L1?

The paper is organized as follows. In Section 2 we present a synopsis of the instrumentation. We begin our analysis with an overview of the homologous events on 2012 March 7 (Section 3) and then use multipoint energetic proton measurement to determine the proton release time for the different observers (Section 4). Next, we examine the relation of the particle release time at each observer to the evolution of the EUV waves (Section 7.1) and the extent of the WL shock (Section 7.2). We conclude in Section 9.

2. INSTRUMENTATION

In situ SEP measurements are provided by instruments at three widely separated positions in the heliosphere. At the first Lagrange point (L1-Earth), we use 1.5–140 MeV proton intensities from the *Energetic and Relativistic Nuclei and Electron* (ERNE; Torsti et al. 1995, pp. 505–31) instrument on board *SOHO*. We supplement these observations with data from the Energetic Particle Sensors (EPSs) on board the *Geostationary Operational Environmental Satellites* (*GOES*/EPS; Sauer 1993) and Electron Proton and Helium Instrument (EPHIN; Müller-Mellin et al. 1995) on board *SOHO*. Data away from the Sun–Earth line are provided by the *STEREO* spacecraft, one ahead of Earth's orbit (*STEREO-A*: *STA*), and the other trailing (*STEREO-B*: *STB*). The SEP instrument suite consists of the High Energy Telescope (HET; von Rosenvinge et al. 2008), which covers energies from 13.6 to 100.0 MeV/n, and the Low Energy Telescope (LET; Mewaldt et al. 2008), with an energy range of 1.8–15.0 MeV/n. The heliographic longitudes of *STB* and *STA* with respect to Earth on March 7 were 117.°6E and 109.°3W, respectively.

For the analysis of EUV waves, we use full-disk EUV images (195 Å filter) from the Extreme Ultraviolet Imager (EUVI) in the Sun–Earth Connection Coronal and Heliospheric Investigation (SECCHI; Howard et al. 2008) instrument suite on board *STEREO*. We also use full-disk EUV images at 193 and 211 Å from the Atmospheric Imaging Assembly (AIA: Lemen et al. 2012) on board *SDO*. For the comparative analysis of the associated WL CMEs and shocks we use data from the *STEREO* coronagraphs (COR1 and COR2) and the Heliospheric Imager instrument (HI1; Eyles et al. 2009). The fields of view (FOVs) of COR1 and COR2 are 1.4–4 $R_\odot$ and 2–15 $R_\odot$, respectively. The COR1 cadence was $\sim$5 minutes, and the COR2 cadence was $\sim$15 minutes.

We also assembled dynamic radio spectra using data from the *STEREO*/WAVES (SWAVES) instrument (Bougeret et al. 2008), with 1-minute resolution in the frequency range from 2.6 kHz to 16.075 MHz, and from the Radio Solar Telescope Network (RSTN; Guidice et al. 1981), with 3 s resolution in the frequency range from 25 to 180 MHz.

3. THE TWIN ERUPTIONS OF 2012 MARCH 7

3.1. Active Region and Flares

The SEP event was associated with two near-simultaneous flare/CME events that occurred only 1 hr apart within the same active region (AR) on 2012 March 7. The center position of the host AR 11429 was N16°E29° on March 7 00:00 UT and was a highly magnetic complex region ($\beta\gamma\delta$ of the Hale classification). The first flare was an X5.4 from N18°E31°, starting at 00:02 UT and peaking at 00:24 UT. The second, X1.4 flare started at 01:05 UT and peaked at 01:14 UT. It was located at N15°E26°. Figure 1 shows the location of AR 11429

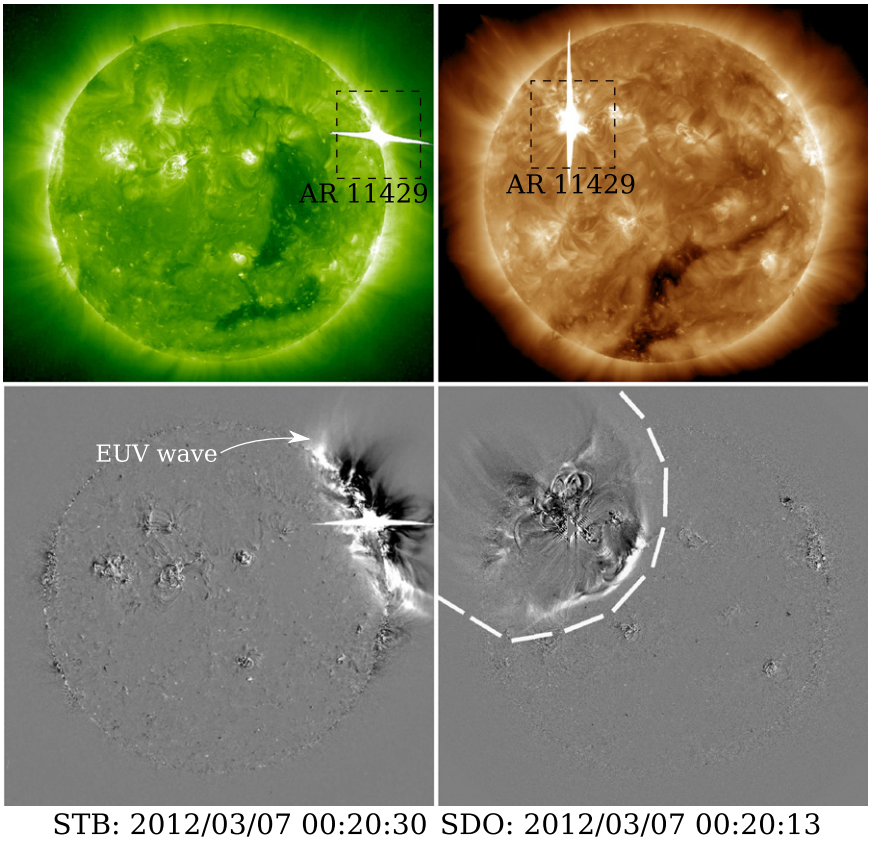

Figure 1. Top panels: EUV images during the first flare (2012 March 7 at 00:20 UT) recorded from *STB* (top left) at 195 Å and AIA (top right) at 193 Å. The dashed boxes outline the location of AR 11429. Bottom panels: running-difference images. A part of the expanding EUV wave is labeled with an arrow (left panel) and outlined with the dashed line (right panel).

in EUV images from *STB* and *SDO*. The events were behind the limb for *STA*. The solar, heliospheric, and magnetospheric activity associated with these events is described in detail in Patsourakos et al. (2016). In the following, we present only the information relevant to this paper for completeness starting with Table 1, which contains a summary of the sequence of events during 2012 March 7.

3.2. EUV Waves, WL CMEs, and Shocks

Two EUV waves, EUV-W1 and EUV-W2 hereafter, were launched in connection with the two flares. In Figure 1 we mark EUV-W1 at *STB* (195 Å; bottom left) and in *SDO* (195 Å; bottom right) running-difference images. EUV-W1 was first observed at ∼00:12 UT, while EUV-W2 was first observed 1 hr later at ∼01:02 UT. Both waves followed a similar southwestern path. A detailed analysis of both EUV waves is presented in Section 7.1.

Additionally, WL coronagraph observations recorded CMEs CME1 and CME2. In Figure 2 we show COR2B/A (left and right) and *SOHO*/LASCO (middle) observations of CME1. It erupted off the western COR2B limb and off the eastern LASCO limb. It was also clearly observed by COR2A. CME1 first appeared at ∼00:16 UT in COR1B and at ∼00:40 UT in COR2B. The height–time measurements from *SOHO*/LASCO observations of CME1 correspond to a speed of 2684 km s^{-1} according to the CDAW CME catalog (Yashiro et al. 2004). An analysis of the CME1 kinematics with triangulation techniques by Liu et al. (2013) resulted in a similar peak speed of about 2400 km s^{-1}. Their analysis,

Table 1
Sequence of Events during 2012 March 7

Episode	Observ.	Characteristic	Time (UT)
Flare	*GOES*-15	Start	00:02
Coronal Loops	AIA/211	Slowly Rising	00:07
EUV wave	AIA/211	Formation	00:12
CME	LASCO	Lift Off (H–T extrapolation)	00:16
CME	COR1B	1st Appearance	00:16
Type III	RSTN	Start—180 MHz	00:17
Flare	*GOES*-15	Maximum—X5.6	00:24
CME	LASCO/C2	1st Appearance	00:24
μwaves[a]	Learmonth	Maximum–5 GHz	00:26
Type II	SWaves	Start—16 MHz	00:30
CME	COR2B	1st Appearance	00:39
CME	LASCO/C3	1st Appearance	00:42
CME	COR2B	WLS signatures	00:54
EUV wave	AIA/211	Formation	01:02
CME	LASCO	Lift Off (H–T extrapolation)	01:04
Flare	*GOES*-15	Start	01:05
Type II	RSTN	Start—50 MHz	01:12
CME	COR1B	1st Appearance	01:11
Type IV	RSTN	Start—180 MHz	01:11
Flare	*GOES*-15	Maximum—X1.4	01:14
μwaves[a]	Learmonth	Maximum—5 GHz	01:14
CME	COR2B	1st Appearance	01:25
CME	LASCO/C3	1st Appearance	01:30

Note.
[a] Microwave radio emission.

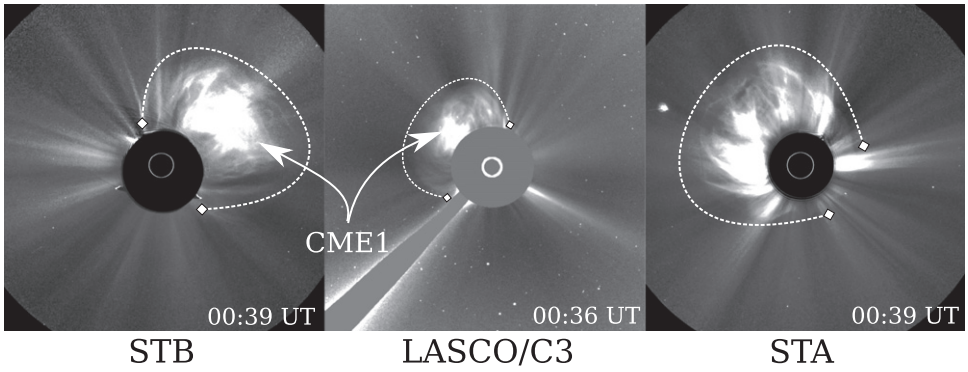

Figure 2. Images of the outer corona from COR2 (left from *STB* and right from *STA*) and LASCO/C3 (middle) during the expansion of the first CME on 2012 March 7. The CME is marked with arrows, and the approximate shock extent is denoted with the dashed lines.

however, does not separate CME1 from its overlying shock. Kwon et al. (2014) employed a 3D reconstruction of CME1 morphology and showed that the CME is composed of two distinct structures: an outermost bubble propagating at ~2800 km s^{-1} followed by a flux-rope-like main body propagating at ~2400 km s^{-1}.

CME2 was quite more difficult to detect as it erupted in a corona disturbed by CME1. However, it was visible from all three viewpoints. Its first appearance in COR1B was at ~01:11 UT and in COR2A was at ~01:25 UT with a speed of 1825 km s^{-1} according to the CDAW CME catalog. Clearly, CME1 and CME2 were unlikely to interact since CME2 was slower and erupted 1 hr later than CME1. In addition, the 3D modeling of the two CMEs by Patsourakos et al. (2016) showed that the CMEs propagated in different directions. Lastly, we did not find any radio signatures in the composite radio spectra (see Section 3.5) to support a CME–CME interaction (Gopalswamy et al. 2001; Martínez Oliveros et al. 2012).

A shock accompanied CME1, shock1 hereafter (Kwon et al. 2014; Patsourakos et al. 2016). It manifests itself as a bright front around the CME (Vourlidas et al. 2003; Ontiveros & Vourlidas 2009) and via deflections of streamers eastward of CME1 seen in COR1B at ~00:36 UT and in COR2B at ~00:54 UT (Figure 2). We could not identify any shock signatures associated with CME2. This does not necessarily imply the lack of a shock associated with CME2. The disturbed background from CME1 makes visual detection difficult and may alter the ambient Alfvénic profile encountered by CME2. Further evidence for shock-related signatures during CME1 and CME2 will be presented in Section 3.5 from the corresponding radio signatures.

3.3. Solar Energetic Protons

The SEP event was the largest event detected at either *STEREO* spacecraft or at Earth during 2012 March. This was a particularly active month highlighted by a barrage of powerful events. The most pronounced were the events on March 7, 9, 18, 21, and 24 (see Table 3 in Papaioannou et al. 2014). The 6–10 MeV proton peak fluxes were enhanced by more than ~4–5 orders of magnitude above the background level ($I_b \sim 10^{-3}$ to 10^{-2} /cm^2 s sr MeV).

Figure 3 summarizes the time history of proton intensities, around the onset of the March 7 SEP event in *STA-B* (60–100 MeV) and *SOHO*/ERNE (80.2–101 MeV) supplemented by *GOES* SXRs, CME height–time measurements from

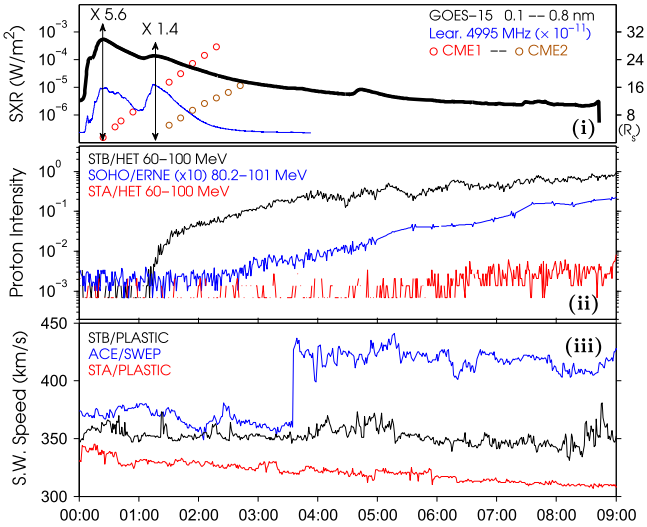

Figure 3. Time history of X-ray emission, solar energetic protons, and solar-wind speed near the onset of the SEP event on 2012 March 7. From top to bottom: (i) SXR flux at 0.1–0.8 nm (*GOES* satellites, NOAA), radio flux at 4.995 GHz (RSTN network, Learmonth), and CME height–time measurements (CDAW); (ii) particle recording from *STB* and *STA* at 60–100 MeV and *SOHO*/ERNE at 80.2–101 MeV; and (iii) solar-wind velocity (*STB*, *STA*, and *ACE*/SWEPAM). This time interval includes the two solar flares and the onset of the SEP event.

CDAW, and solar-wind velocity from *STB-A* and the *Advanced Composition Explorer* (*ACE*)/SWEP instrument. A prompt increase in proton intensity was recorded at *STB* (60–100 MeV) around 01:15 UT, while at L1 the 80–101 MeV particle intensity increased later at 02:40 UT. The proton intensities were more enhanced at *STB* compared to the L1 observations (Figure 3(ii)). At *STA* the event was weak starting after 05:15 UT at 60–100 MeV.

Aspects of this SEP event have been discussed elsewhere (Richardson et al. 2014, see their Figure 9). The event was observed by *MESSENGER* (Lario et al. 2013) orbiting Mercury at heliocentric distance 0.3 au (−57° longitude at heliocentric Earth equatorial coordinate system) and by the *Mars Science Laboratory* spacecraft, en route to Mars at a distance of 1.2 au (Zeitlin et al. 2013).

3.4. Solar-wind Speed

As seen in Figure 3(iii), the solar-wind speed measured by *STB*/PLASTIC ranged between 350 and 370 km s^{-1} (00:00 UT to 09:00 UT on 2012 March 7). At *STA*, the solar-wind speed

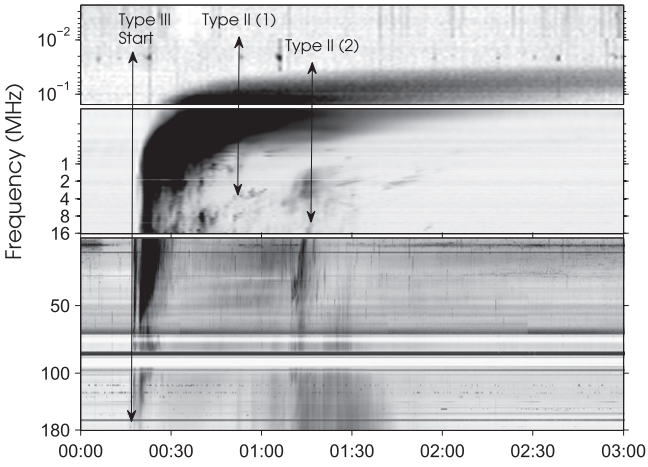

Figure 4. Radio spectra at dm–m waves (*STB*/SWAVES and RSTN) on 2012 March 7 from 00:00 to 03:00 UT.

was declining during the day, measuring ∼340 km s^{-1} at the start of the SEP event. At L1 the solar-wind speed ranged between 350 and 440 km s^{-1} (00:00 UT to 09:00 UT on 2012 March 7). Additionally, the *SOHO*/CELIAS/MTOF Proton Monitor captured two shock-like structures: one at ∼03:40 UT and another at 12:00 UT (not shown here). The latter feature at 12:00 UT was likely associated with the second CME from March 5 (see Magdalenić et al. 2014). On March 8 an IP shock reached Earth at around 10:30 UT, followed, a few hours later, by an interplanetary CME (ICME). The ICME triggered a major geomagnetic storm (minimum Dst ∼ −131 nT). We use these solar-wind measurements to estimate the Parker spiral connection points (in Section 7.1).

3.5. Solar and IP Radio Emission

Flares, CMEs, and SEP events are commonly accompanied by various types of transient solar radio emissions, e.g., type III, II, and IV (e.g., Kouloumvakos et al. 2015, and references therein). The emissions are usually interpreted as signatures of electron beams (type IIIs), as electrons accelerated in shock waves (type IIs), or as electrons confined (type IV) in closed loop structures. Figure 4 shows the composite radio spectra from *STB*/SWAVES between 2.6 kHz and 16.025 MHz (upper part) and RSTN between 25 and 180 MHz (lower part).

The dynamic spectrum shows the start of a type III radio burst at ∼00:17 UT (at ∼180 MHz), which could be ascribed to electrons accelerated at magnetic reconnection sites escaping via open field lines, and is related to the SXR maximum of the first event. A type II radio burst at ∼00:30 UT (Figure 4, at ∼16 MHz) signals shock formation in the corona. Additionally, Schmidt et al. (2014), using a magnetohydrodynamic (MHD) simulation of this event combined with radio radiation theory, predicted a type II burst starting at 00:21 UT (at 15 MHz) and ending at 04:10 UT (at 0.1 MHz). The radio emission modeled in the simulation is not obvious in the observed radio spectrum, though it is possible that a part of it is obscured by the strong type III bursts.

The type II radio burst drifted toward lower frequencies, ending at 2 MHz (fundamental), and it probably exhibited both fundamental and harmonic emission from 4 to 8 MHz (at ∼00:50 UT). It is not clear whether the type II has a counterpart in decametric or metric radio waves because of the intense bands of type III emission that could mask any other radio emission. From the start of the type II radio burst we find shock1's onset at ∼00:30 UT. In a more extended and enhanced view of the radio spectra we identified a long duration IP type II emission probably extending to the arrival of the shock at Earth on March 8. Moreover, a slowly drifting continuum (possibly a type IV) was recorded in a broad frequency range (16–180 MHz) from 00:30 UT to 01:15 UT.

The second event is associated with a type II radio burst that started at ∼01:12 UT (∼50 MHz fundamental) and a type IV that started almost simultaneously with the type II and lasted ∼45 minutes; no IP type III is observed during or after the second event. The feature labeled "type II (2)" in Figure 4 should not be confused with a type III-like emission; from a more detailed view of this time interval we found that this feature has a pronounced component with fundamental–harmonic relation and a drift consistent with type II emission and not with type III. The presence of the type IV radio burst and the absence of type III suggests that the electrons in the second event were accelerated and remained confined for some time in low coronal structures. We did not identify any signatures indicating CME–CME interaction.

We used the microwave flux from Learmonth (RSTN network) as a proxy to the hard X-ray (HXR) emission (e.g., White et al. 2011, and references therein). Microwave emission (∼5 GHz) comes from low coronal heights (∼ 10^5 km) and is incoherent gyrosynchrotron emission from mildly relativistic electrons. The microwave flux showed two peaks that are associated with the maxima of the two flares: one peak at ∼00:26:33 UT (9569 SFU at ∼5 GHz) and a second peak at ∼01:14:37 UT (12,723 SFU at ∼5 GHz). Supporting observations were reported by Ajello et al. (2014) from the HXR count rates of the Gamma-ray Burst Monitor on board the *Fermi* Large Area Telescope (LAT). GBM also showed two peaks associated with the two flares. Moreover, Ajello et al. (2014) reported that *Fermi* LAT detected gamma rays up to 4 GeV during the event from a site coinciding with the location of AR 11429. Although the gamma-ray and microwave observations suggest two episodes of energy release within the flaring regions, none of the *STB*/A or L1 particle intensity profiles revealed evidence of a second resolved proton acceleration in the form of a distinct intensity peak.

From the analysis of the solar and IP radio emissions, and namely from the presence of two metric type II radio bursts and two peaks in HXR and microwave emissions, we conclude that there was an associated shock for both CMEs in the low corona. However, there was only one IP type II and hence a single shock that made it to Earth. This is consistent with the WL observations discussed in Section 3.2. We will search for the driver of this shock in Section 7.

4. ESTIMATE OF SOLAR ENERGETIC PROTON RELEASE TIMES

4.1. Proton Onset Times

We used the Poisson-CUSUM method to determine proton onset times for *STB*, L1, and *STA* and applied it to all available energy channels. The CUSUM quality-control schemes were proposed by Page (1954) and are widely used in fields such as industry and medical research. By the CUSUM definition, the onset time of an event, for a given energy channel, is the instant when the signal has a systematic change of its mean value compared to a pre-event background mean. We use the two-

sigma-shift criterion (Huttunen-Heikinmaa et al. 2005) to identify when a transition in the mean value has occurred. CUSUM schemes are efficient in detecting small shifts in the mean of a process.

The Poisson-CUSUM method is usually sensitive to departures of the observed values (Y_i) from the pre-event background mean value (μ_α). Therefore, it is necessary to have accurate and robust evaluations of the latter. However, this is not always possible in the presence of a contaminated pre-event background. Moreover, the a priori selection of the temporal interval where μ_α is evaluated may introduce significant uncertainties in the proton onset evaluation.

We use a Monte Carlo method that evaluates the possible errors introduced in the onset determination from small changes in μ_α. This method, proposed by Kouloumvakos et al. (2015), relies on the repeated calculation of μ_α at a random sampling of pre-event time intervals. We find a new onset time from the CUSUM method for each calculated μ_α. This repetitive process produces a collection of estimated onset times that are normally distributed around a certain fixed value. The maximum of the distribution corresponds to the proton onset time with the highest probability and its full width at $\sim 3\sigma$ to the onset time uncertainty.

We applied the Poisson-CUSUM method to *STB* proton data to determine the proton onset times. ERNE proton data after ~05:00 UT were intermittent owing to the operational mode of ERNE, which favors the heavy-ion data, making it difficult to determine an accurate onset time for the low-energy channels. We therefore rejected from our analysis the energy channels from 1.58 to 10.1 MeV.

4.2. Velocity Dispersion Analysis

A commonly used method (e.g., Huttunen-Heikinmaa et al. 2005; Vainio et al. 2013) for the determination of particle release times and their apparent IP travel paths is the velocity dispersion analysis (VDA). Given that less energetic particles arrive at a given observing point later than the more energetic ones, this implies a velocity-dependent time dispersion of the first particle detections. The VDA method relies on the following assumptions: (1) the first energetic particles are simultaneously released from a small acceleration site in the solar corona, and (2) the first particles observed at the spacecraft propagate scatter-free in the IP medium. From the linear relationship between the proton onset time of the first arriving particles and the inverse particle velocity, which is a function of the particle energy, we estimate the IP distance traveled by the energetic particles from the slope of the linear fit and the solar release time from the intercept with the horizontal axis.

Following Kouloumvakos et al. (2015), we considered the uncertainties of the proton onset times (δt) determined from the Monte Carlo analysis (Section 4.1) and the uncertainties of the inverse velocities determined from the width of the corresponding energy bins. Although the ordinary least-squares (OLS) method is widely used, the estimation of the relative error in proton release and path length with the OLS method is not straightforward because of the error in both proton onset times and inverse velocities. The OLS method does not provide an unbiased best-fit line when data have inherent uncertainties in more than one regression variable and the uncertainty varies from point to point. Therefore, we use the method of York et al. (2004) that applies the maximum likelihood estimation (MLE) to the determination of slopes, intercepts, and standard errors of a number of data sets.

In Figure 5 we display the VDAs for *STB* (i), L1 (ii), and *STA* (ii) and we show the calculated proton release times and the apparent path lengths with their relative errors for both the OLS and MLE method. At *STB* (see Figure 5(i)) the proton release time was estimated at 00:25 UT ± 4 minutes with the MLE method. The corresponding path length was 2.35 ± 0.08 au. At L1 (see Figure 5(ii)), a proton release time at 01:27 UT ± 25 minutes was obtained with the MLE method. To reduce the release time uncertainty, we complement the VDA with data from *SOHO*/EPHIN and the *GOES* 13 satellite. Although the *GOES* high-energy channels contaminate the low-energy ones, it is possible to have a fairly good onset time in the high-energy channels. From *GOES* and *SOHO*/EPHIN the release time was found slightly later at 01:30 UT ± 22 minutes (MLE). From a sample of 107 SEP events Vainio et al. (2013, see their Figure 1) have shown that the apparent path length values typically range within 1–3 au. In our case the apparent proton path lengths at L1 were extremely high, 5.58 ± 0.82 au and 5.43 ± 0.72 au, respectively; therefore, we could not trust the results of the VDA. This might be caused by the pre-event background affecting the proton onset time determination in several channels and especially the low-energy channels. We can only say that the proton release time estimated from measurements at L1 is significantly delayed compared to *STB* (~1 hr).

The proton intensities in high-energy channels of *STA* (see Figure 5(iii)) are close to the background levels and show a nondispersive relation; in low energies only six channels were available. From this limited set we found an apparent path length of 1.68 ± 1.30 au and a delayed proton release time, with respect to *STB*, at 02:51 UT with a high uncertainty of ±1.5 hr. In Table 2 we summarize the calculated proton release times and path lengths from the VDA.

4.3. Time-shifting Analysis

To complement our VDA analysis of the previous section, we performed a time-shifting analysis (TSA). This method shifts in time the proton onset times in a particular energy channel, to determine the proton release time at the Sun (e.g., Vainio et al. 2013). This method assumes that the first arriving particles propagated scatter-free until their detection point; therefore, TSA best applies in high-energy channels and gives an estimate of the latest possible release time of protons.

Instead of using the apparent path length obtained from the VDA, we used the nominal Parker spiral length, L, which is computed for a solar-wind speed u_{sw} before the event. The nominal path length, L, can be estimated from the equation $L(u_{sw}) = z(r) - z(R_\odot)$, where $z(r)$ is the arc length of an Archimedean spiral from the center of the Sun to a radial distance r and is given by

$$z(r) = \frac{a}{2}\left[\ln\left(\frac{r}{a} + \sqrt{1 + \frac{r^2}{a^2}}\right) + \frac{r}{a}\sqrt{1 + \frac{r^2}{a^2}}\right], \qquad (1)$$

where $a = v_{sw}/\omega$ and ω is the solar angular rotation speed. L can be generally considered as a good approximation to the distance traveled by the particles. The nominal Parker spiral length is typically around ~1.2 au assuming a $v_{sw} = 375\ \mathrm{km\ s^{-1}}$. However, several studies have reported longer path lengths (e.g., Masson et al. 2012; Vainio

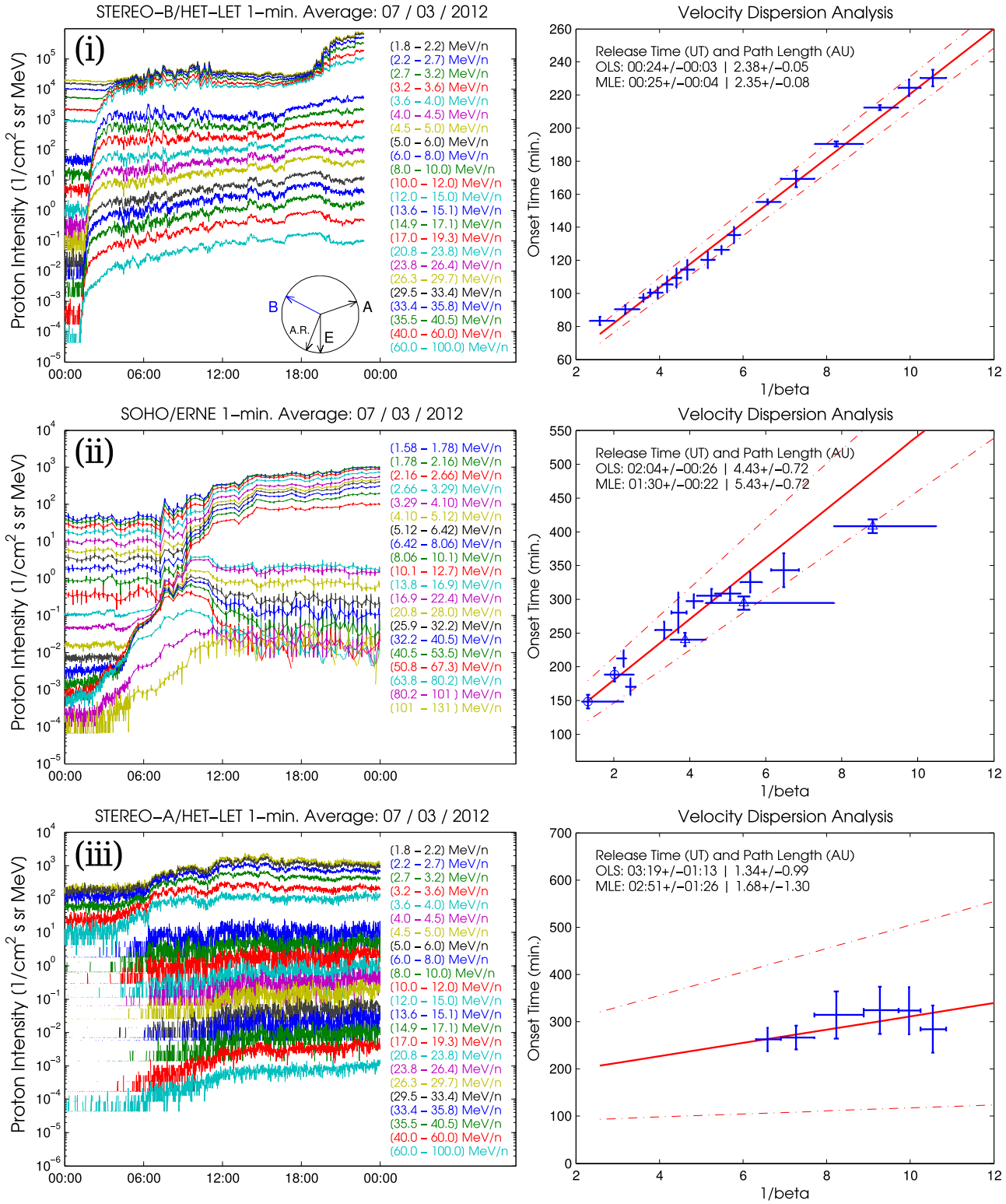

Figure 5. Left panels, top to bottom: proton intensities from (i) *STB*, (ii) *SOHO*/ERNE, and (iii) *STA* in all available energy channels during 2012 March 7. In the top left panel, the embedded compass shows the relative positions of the *STEREO* spacecraft, Earth, and the longitude of AR 11429. Right panels: velocity dispersion analysis for (i)–(iii). The onset timescale starts at the beginning of 2012 March 7. The proton onset times are marked with blue error bars and the MLE linear fit and its uncertainty with the red solid and dot-dashed lines, respectively. In the middle right panel, the *GOES* and *SOHO*/EPHIN proton onset times are marked with circles and triangles, respectively. The resulting proton release times and their travel path length from the OLS and MLE method are noted in every panel.

et al. 2013). One possibility is that ICMEs may distort the IP magnetic field; therefore, the energetic particles are traveling along considerably greater path lengths.

We estimated the proton release times with TSA using the highest available energy channels in the range from 60 to 100 MeV for the *STEREO*/HET and the corresponding energy

Table 2
Proton Release Times from VDA and TSA

Observ.	Time (UT)	Path Length (au)
VDA method:		
STB	00:25 ± 04 minutes	2.35 ± 0.08
ERNE	01:30 ± 22 minutes	5.43 ± 0.72[a]
STA	02:51 ± 1.5 hr[b]	1.68 ± 1.30
TSA method:		
STB	00:22 ± 03 minutes	2.44
	00:48 ± 03 minutes	1.18
ERNE	01:54 ± 12 minutes	2.36
	02:18 ± 12 minutes	1.14
STA	04:19 ± 15 minutes	2.59
	04:47 ± 15 minutes	1.29

Notes.
[a] Extremely high travel path length.
[b] Uncertain proton release time.

range from 80.2 to 101 MeV for *SOHO*/ERNE. We purposely applied the TSA method on the high-energy channels to ensure that the proton onset time will be least affected by scattering. The nominal path length in each case has been calculated using solar-wind measurements from *STEREO*/PLASTIC and *ACE*/SWEP during the event (see Figure 3(iii)). For *STA* we applied TSA in the 15-minute average data because the estimated signal-to-noise ratio at the high-energy channels was low ($\ll 1$) and there are intervals with no counts before the event. We show both the TSA and VDA results in Table 2.

In Figure 6 we present the proton intensity profiles at *STB*/A and *SOHO*/ERNE combined with the results from TSA. The red dashed line and the green dashed line mark the proton onset time and the proton release time derived from TSA, respectively. Additionally, we show with the green shaded area an estimate of earliest possible proton release time; in this calculation we used a path length twice the value of our calculated nominal path length (s) (e.g., Vainio et al. 2013, see their Figures 2 and 5). This assumption is also consistent with the studies discussed in the previous paragraph and sets a generous limit on the *earliest* proton release time. The results of the TSA show that for *STB* the proton release was between 00:22 UT ($s = 2.44$ au) and 00:48 UT ($L = 1.22$ au), whereas for *SOHO*/ERNE it was between 01:54 UT ($s = 2.36$ au) and 02:18 UT ($L = 1.18$ au). At *STA* the proton release time was between 04:19 ($L = 2.59$ au) and 04:47 UT ($L = 1.29$ au). We conclude that the proton release time computed from TSA for *STB* is consistent with the release time deduced by the VDA. Moreover, TSA has given further evidence in support of the delayed release of protons detected at L1 and *STA*.

5. ELEMENTAL AND ISOTOPIC ABUNDANCES AND ENERGY SPECTRA

SEP elemental and isotopic abundance ratios and the ^{3}He/^{4}He and Fe/O ratio, in particular, provide valuable information on the underling physical processes of particle acceleration and release throughout the heliosphere (e.g., Reames 1999). Impulsive events have 1000-fold enhancements of ^{3}He/^{4}He ratio and 10-fold enhancements of heavy-element ratio, Fe/O, compared to the abundance ratio in the corona or solar wind. The corresponding enhancements of

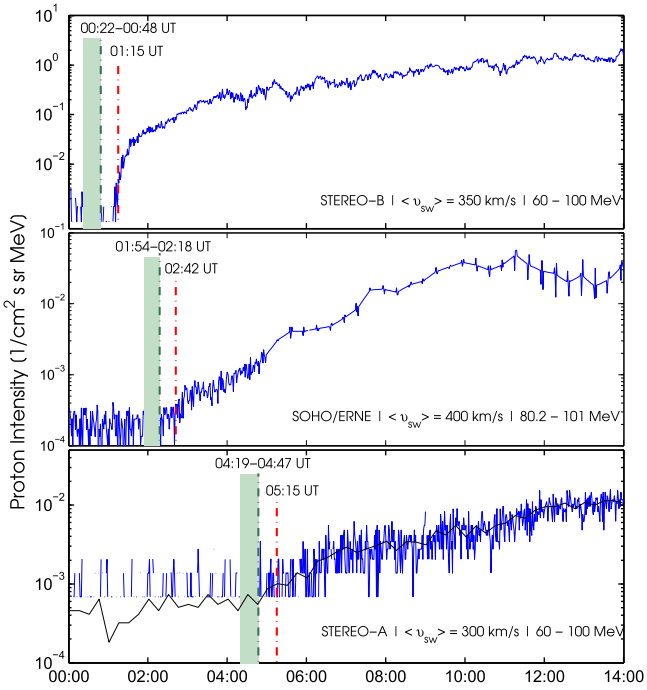

Figure 6. Time-shifting analysis at *STB*/*STA* (top/bottom) and *SOHO*/ERNE (middle) for the energy ranges 60–100 MeV and 80.2–101 MeV, respectively. The energetic particle observations are represented with the blue line. We represent the proton onset time with the red dashed line and the proton release time with the green dashed line. The green shaded area denotes the time interval in which the proton release time could shift if we had used a higher value for the path length.

element ratio for the gradual events are ~10 for ^{3}He/^{4}He and ~0.1 for Fe/O (e.g., Reames 2013).

Using elemental and isotopic data, we hereby elucidate the role of flare and shock in the particle release process. We used particle data from *STB* and *ACE* spacecraft, in a broad energy range, from 0.1 to 100 MeV/n. We used L1 measurements by the Ultra Low Energy Isotope Spectrometer (Mason et al. 1998) and the Solar Isotope Spectrometer (Stone et al. 1998) on board *ACE* and the Energetic Particles: Acceleration, Composition and Transport/Low Energy Matrix Telescope (EPACT/LEMT) on board *Wind*. Particle measurements from *STB* were obtained by the Suprathermal Ion Telescope (SIT; Mason et al. 2008) detector and the LET (Mewaldt et al. 2008).

In Figure 7 we present the energy spectra of ^{4}He, ^{3}He, ^{16}O, and Fe between 0.1 and 100 MeV/n that were computed using *STB* (open circles) and *ACE* (opened triangles) measurements during the SEP event, from March 7 00:00 UT to March 8 09:00 UT. The time interval considered for the energy spectra allows us to capture the initial composition of the SEP event and does not contain the shock passage at *STB* or Earth to avoid the drop of the Fe/O ratios to nominal values after the shock passes. However, we note that a contamination from the March 5 CME event at the lower-energy channels cannot be excluded. From the chemical elements' energy spectra we determined the abundance ratios of ^{3}He/^{4}He and Fe/O in each case. We mostly trust the ratios in the 1 MeV/n and 10 MeV/n range (Reames & Ng 2004; Reames 2014). For energies below 1 MeV/n the particle intensity may be strongly affected by a transport process, while above 10 MeV/n energy-dependent differences in the trapping and acceleration of ions in the source region might become important (e.g., Reames &

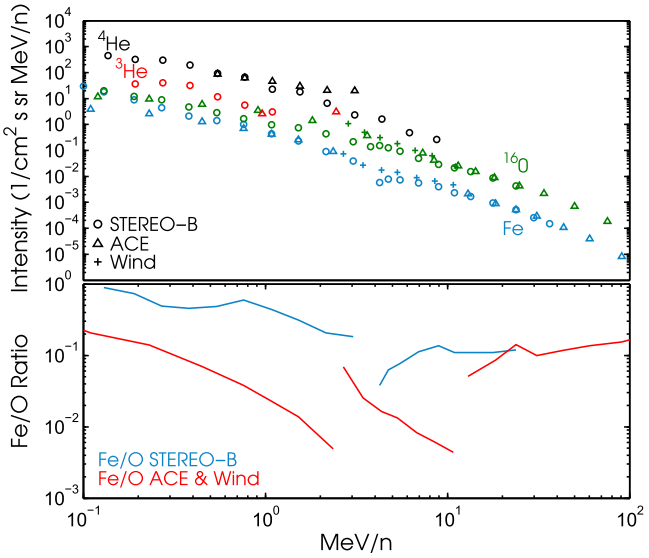

Figure 7. Top: energy spectra of ^{4}He (black), ^{3}He (red), ^{16}O (green), and Fe (blue) in the energy range from 0.1 to 100 MeV/n, computed by averaging *STB* (open circles) and L1 (*ACE*: opened triangles; *Wind*: plus signs) measurements during the SEP event, from March 7 00:00 UT to March 8 00:00 UT. Bottom: Fe/O ratio as a function of energy for *STB* and L1 in the same energy range and time interval as the top panel.

(An animation of this figure is available.)

Ng 2004). However, Cane et al. (2006) managed to distinguish impulsive from gradual SEP events by using Fe/O ratios from 25 to 80 MeV/n.

The Fe/O ratio in the energy range between 1 and 10 MeV/n is 0.018 at *ACE* and *Wind* and 0.24 at *STB*. The above Fe/O ratios are consistent with the gradual SEP Fe/O average values of ∼0.1 shown by Reames (1999, 2014) and Reames & Ng (2004). Additionally, we examined the energy spectra of the Fe/O ratio (see Figure 7 bottom) for both *STB* and L1 (*ACE*–*Wind*). At *STB* we found that the Fe/O ratio decreases with increasing energy, while at the combined energy spectra of *ACE* and *Wind* their energy spectra decrease in the energy range between 0.1 and 10 MeV/n, and thereafter above 10 MeV/n the Fe/O increases.

In addition to the Fe/O ratio, we determined the ^{3}He/^{4}He ratio for *STB* and *ACE*. During March 7, no ^{4}He intensity increase was observed by *STB*/SIT below ∼1 MeV/n possibly because the preexisting background was high. For ^{3}He no measurements were available above ∼1.5 MeV/n, but an intensity increase was observed at 0.2–1 MeV/n around 17:00–18:00 UT on March 7. At *STB*/LET, the ^{4}He intensities at ∼10 MeV/n started to increase significantly above background levels at around 02:45 UT on March 7, but no measurements for ^{3}He were available. At *ACE*, ^{4}He started to increase after 04:00 UT on March 7, while ^{3}He was close to the background values until 10:00 UT and started to slightly increase afterward. From the available measurements we found that the ^{3}He/^{4}He ratio at *STB* is ∼0.09–0.13 and ∼0.04 at *ACE*. At *STB* the ^{3}He/^{4}He ratio is close to the limit of Reames (2013) for impulsive events; therefore, a contribution of flare-related particle release cannot be excluded. At *ACE* there is no clear evidence for a ^{3}He enrichment in support of a flare-related particle release, which is consistent with the poor magnetic connectivity of *ACE* to the flare site.

6. THE MARCH 7 SOLAR ENERGETIC ELECTRON EVENTS

In association with the solar energetic proton event, an increase at the energetic electron intensities was recorded over a wide longitudinal extent (*STB*/*A* and L1). Using electron data from *STB*/*A*, *SOHO*/EPHIN, *Wind*/3DP, and *ACE*, we hereby examine the connection of energetic electrons with the *major* proton event of March 7. We first calculate the electron release times using the VDA and TSA and compare them with the proton release times presented in the previous section.

At *STB* a prompt increase in electron intensity was recorded at 1.4–2.8 MeV around 00:51 UT on March 7. At L1 the high background from previous electron events makes the determination of the electron onset times difficult. In both *Wind*/3DP and *ACE* the energetic electron intensities started to slowly rise well before the start of the first flare; the constantly changing background makes it difficult to distinguish between the first arriving energetic electrons and the pre-event values. At *SOHO*/EPHIN there is a data gap in the pre-event interval and after 12:00 UT of March 7, but the start of the energetic electron event was clearly recorded at around 02:03 UT on March 7, in the energy range 2.6–6.1 MeV. At *STA* the first arriving energetic electrons were recorded at 1.4–2.8 MeV around 01:25 UT. A first remark on the energetic electron onset times is that at *STA* the electron onset precedes the proton onset by 3 hr.

We estimated the electron release time in each observing point using the VDA (see Section 4.2) and TSA (see Section 4.3). At *STB* the 1.4–2.8 MeV electron release time was found from VDA at 00:33 UT ± 6 minutes (MLE method) and from TSA at 00:36 ± 5 minutes. The corresponding path length was 1.08 ± 0.17 au from the VDA, while in the TSA we used the *STB*'s nominal path length of 1.22 au. At L1 it was not possible to perform VDA because the contamination in electron intensities made the calculation of the onset times ambiguous. However, from the electron data of *SOHO*/EPHIN we manage to perform TSA in the energy range 2.64–6.18 MeV; the electron release time was found at 01:51 UT ± 5 minutes using the nominal path length of 1.18 au. AT *STA* we performed VDA, but the resulting travel path length and consequently the release time were unrealistic because the dispersion of the electron onset times was too low. From the TSA of 1.4–2.8 Mev electrons at *STA* we found that the electron release was at 01:09 UT ± 10 minutes using the nominal path length of 1.29 au.

From the analysis of electron data at *STB*/*A* and L1 and the estimated electron release times we found that the electron release compared with the proton release was (1) slightly delayed (∼10 minutes) at *STB*, (2) simultaneous or delayed at L1 depending on the proton path length, and (3) significantly leading (∼3 hr) at *STA*. From the timing of particle release times at both *STB* and L1 we conclude that there is a clear connection between the solar energetic proton event and the energetic electron event. However, based on the relative timing between the electron and the proton event at *STA*, it is uncertain why the particles arrived at *STA* with such a high time

difference. The source of the electron event at *STA* is discussed in Section 9.

7. CME AND SHOCK EVOLUTION

Since SEPs follow the magnetic field lines to their detection point, tracing these lines sunward would allow us to locate their source. Generally speaking, the solar source of the particles is located by assuming magnetic field lines following a Parker spiral corresponding to a given solar-wind speed, the flare location, the evolution of the EUV wave, and the CME-driven shock propagation direction and extent. In this section, we examine whether the EUV wave and/or WL CME shock can account for the release times and longitudinal spread of the SEPs.

7.1. Coronal EUV Observations

First, we derive the arrival times of the observed EUV waves to the footpoints of field lines connecting to *STB* and L1 and compare them with the corresponding proton release times as inferred from the VDA and TSA analysis in Section 4.

We compile a sequence of full-Sun Stonyhurst maps, at ~2 hr intervals starting at 00:00 UT, by assembling images from both EUVIs at 195 Å (~1.2 MK) and the nearest-in-time AIA image at 211 Å (~ 2 MK). We use 211 Å AIA images instead of 193 Å because the EUV wave is more visible in this wavelength. We also correct for differential rotation to eliminate any effects produced from the time difference between the EUVI and AIA images. We convert the full-disk maps to running-difference movies to track more efficiently the evolution of the waves across the solar disk. In Figure 8 we show running-difference snapshots from 00:20 UT to 01:04 UT showing both EUV waves. The complete movie is available in the online version of this paper. Applying the average solar-wind speed (v_{sw}) measured at each spacecraft near the particle onset time (00:00–03:00 UT to exclude the shock detected at L1; see Figure 3) to the Parker spiral model of the IP magnetic field, we calculate the longitudes of the footpoints of field lines connecting to *STB*, L1, and *STA* (Figure 8). We also mark with a horizontal line a 10° uncertainty in the calculated longitudes.

From the synoptic maps we determine the onsets of EUV-W1 and EUV-W2 and track them across the solar disk. EUV-W1 appears at ~00:12 UT around a set of expanding loops in AR 11429. The wave becomes a coherent structure at 00:17 UT. Between 00:20 UT and 00:30 UT EUV-W1 expands at a speed of ~830 km s^{-1}. The EUV-W1 passes over the region that was well connected to *STB* between 00:19 UT and 00:25 UT depending on the assumed solar-wind speed. After 00:32 UT, EUV-W1 becomes diffuse, and its detection is ambiguous after 00:41 UT. The only (indirect) indication of the westward propagation of EUV-W1 is its interaction with coronal structures and neighboring ARs (e.g., Li et al. 2012; Yang et al. 2013) close (~40°) to the L1 magnetically connected region. EUV-W1 can be traced in the east until 00:35 UT. Afterward, interactions with ARs situated from −150° to −130° are indirect indications of a wave presence toward the *STA* well-connected region.

EUV-W2 appears at ~01:02 UT (see Figure 8) around a set of expanding/interconnecting loops between AR 11429 and AR 11430. The EUV-W2 continues to expand with an approximate speed of 430 km s^{-1} along a southwestern direction until ~01:04 UT, when it reaches and interacts with AR 11428. After ~01:05 UT, the wave becomes more diffuse and deforms completely by ~01:13 UT; its detection afterward is ambiguous. The only indirect signature of EUV-W2 is observed at ~01:25 UT near ~30° to ~40° longitude. Based on the EUV-W2 close proximity to the *STB* magnetic footpoint, it is possible that it reached the *STB*'s well-connected longitude.

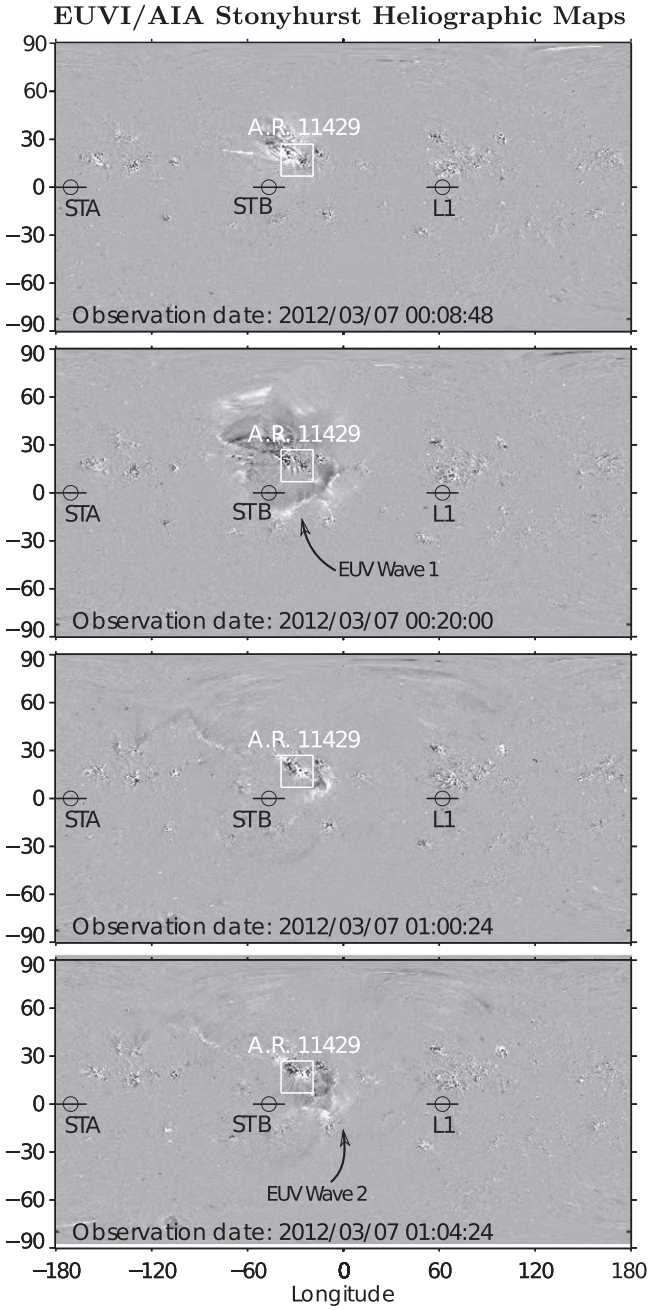

Figure 8. Sequence of full-disk Stonyhurst heliographic maps. They are a composite of *STB* 195 Å, *SDO* 211 Å, and *STA* 195 Å running-difference images. The longitudes of the footpoints of field lines connecting to each observing point are deduced by the Parker model for the evolution of the IP magnetic field and are marked with black circles. The horizontal lines intersecting the circles represent the connection longitude uncertainty. The source region, AR 11429, is enclosed by the white squares.

(An animation of this figure is available.)

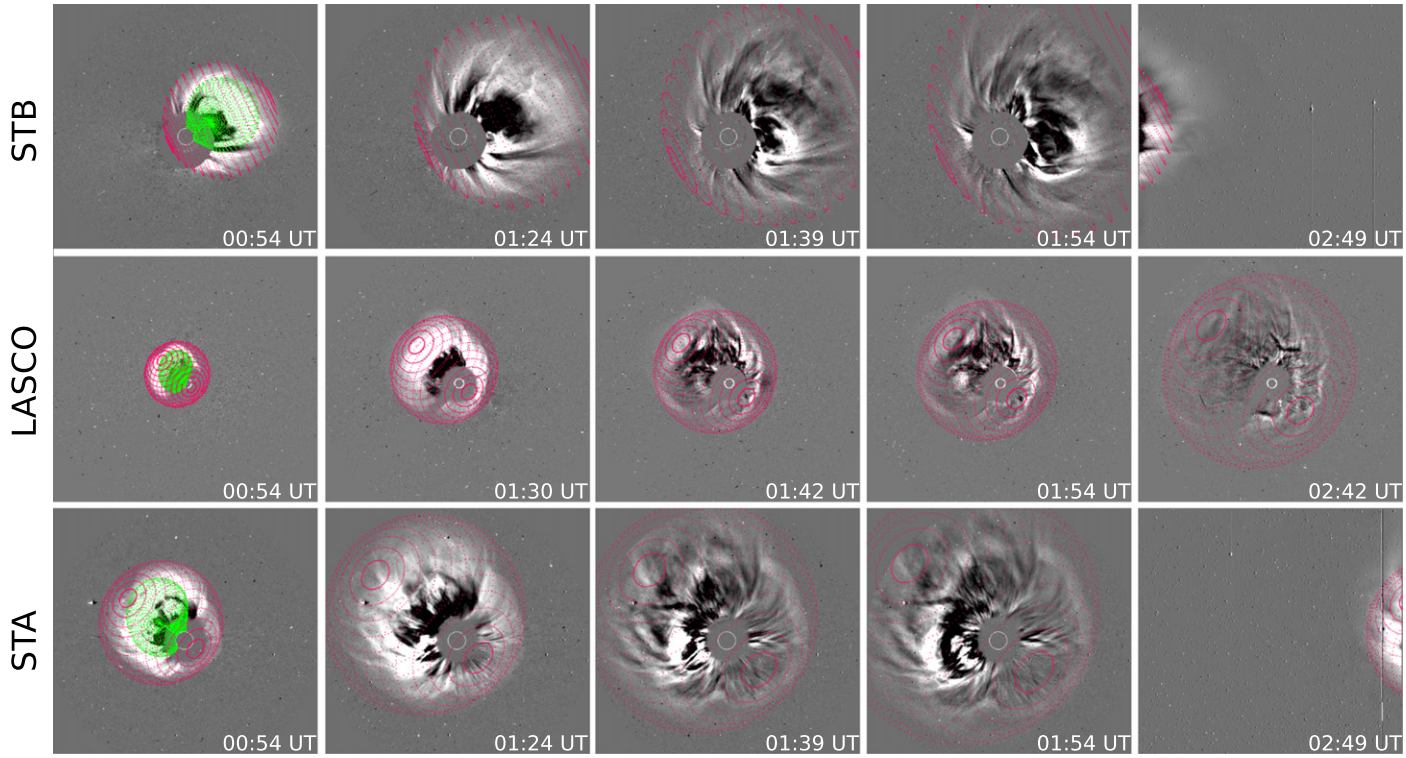

Figure 9. Running-difference images from COR2B/A–HI1B/A (top and bottom rows) and LASCO/C3 (middle) during CME1 expansion. In every frame the red-dotted-line spheroid shows the fitting of the CME shock. In the first column, the green-dotted-line feature shows the CME flux rope fitting.

However, it is unlikely that EUV-W2 reached the L1 and *STA* footpoints.

From the findings of the previous paragraphs and the results of Section 4 we conclude that the proton release time at *STB* (TSA: 00:22 UT; VDA: 00:25 UT) is consistent with the EUV-W1 arrival time at the *STB* footpoint. The ∼5–10-minute time difference could be largely attributed to small shifts of the connection longitude, the uncertainty of the proton release time, or the cadence of the synoptic maps. The proton release time at L1 (TSA: 01:54–02:18 UT) and at *STA* (TSA: 04:24–04:49 UT) cannot be directly compared with the propagation of the EUV waves because there is no evidence that either wave reached the regions connected to L1 and *STA*. Linear extrapolation of the wave tracks to the L1/*STA* footpoints yields arrival times of ∼00:34 UT and ∼00:45 UT for EUV-W1 and of ∼01:30 UT and ∼02:20 UT for EUV-W2, respectively. The arrival times differ significantly (30 minutes and 2 hr, respectively) from the estimated SEP release times.

7.2. Geometrical Fitting of the WL Shock Associated with CME1

Thanks to the multi-viewpoint WL coverage of these events, we can employ forward modeling of the shock and compare its location and extent with the inferred magnetically connected locations of proton release for each spacecraft. The technique is described in Thernisien et al. (2009) and is widely used in SECCHI and LASCO observations. We fit the CME and the shock separately, using a spheroid model (Kwon et al. 2014) for the shock. The CME fits are discussed in Patsourakos et al. (2016).

We use total brightness image triplets (COR1B/C2/COR1A, COR2B/C3/COR2A, and HI1B/C3/HI1A), which lead to more accurate fitting, compared to single- or double-viewpoint ones. We discuss only the WL shock1 modeling. Snapshots from our fittings are given in Figure 9. The shock fittings are plotted as a red wire frame on top of the corresponding COR2B/C3/COR2A (and HI1B/C3/HI1A, in the last frame) triplets. To give some context, the first snapshot is complemented by the CME1 fitting results (green wire frame). Our spheroid fitting reproduces the large-scale appearance and extent of the WL shock quite successfully in all three available viewpoints (*STB*, *SOHO*, *STA*).

We start the WL shock fitting from around 00:20 UT, when CME1 and its shock have clearly emerged above the COR1B and COR1A occulters. We use COR1B/C2/COR1A for the fittings at 00:20 UT and 00:25 UT and COR2B/C3/COR2A from 00:30 UT to 02:30 UT. After 02:00 UT, most of the WL shock exits the COR2B/A FOV. After 02:30 UT, we supplement our analysis with HI1 data using HI1B/C3/HI1A triplets to track the WL shock beyond the COR2B/A FOV. By about 03:30 UT, the shock in LASCO/C3 is too diffuse to unambiguously track; nevertheless, the streamers pushed by the shock give a lower limit of its extent. The HI1 observations allow us to reliably trace the lateral extension of the shock along its the western flank. In Section 8 we use those spheroid fittings to perform a constrained modeling of shock1 in the heliosphere.

Our spheroid fittings yield the shock central longitude (radial direction of the shock nose) and its longitudinal extent (flank extension) on the ecliptic plane. Figure 10 contains the temporal evolution of the shock central longitude (boxes) and longitudinal extent in the ecliptic plane (vertical bars). We also mark the *STB*/L1 magnetically connected regions based on the solar-wind speed close to the SEPs' onset time (solid green lines) and a range of solar-wind speeds (dashed lines) to reflect the solar-wind speed variability at each observing point during

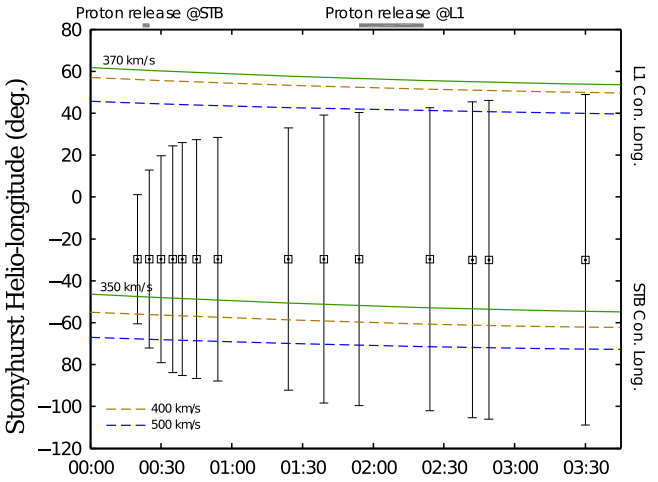

Figure 10. Time evolution of the longitudinal extent of the CME shock (vertical lines) as derived from the spheroid fittings. With the color dashed and solid lines we mark the magnetically connected longitudes for *STB* and L1, respectively, for different solar-wind speed values. The horizontal bars correspond to the estimated proton release times at *STB* and L1 as deduced in Section 4.

(An animation of this figure is available.)

the interval of interest. Our calculation of the connection longitudes takes into account the curvature of the magnetic field lines; therefore, the longitudes does not refer to a fixed height above the photosphere (i.e., $2.5\,R_{\odot}$), but they are estimated using the instantaneous shock heights of the eastern or western flank.

Figure 10 shows that the shock maintains a largely constant direction. Its angular extent is ≈140° at 01:45 UT. From the first fitting at ∼00:20 UT it is clear that the shock eastern flank becomes magnetically connected with *STB* around that time. This is consistent with (1) the coronal EUV wave observations and (2) our estimates for the proton release time for *STB* around 00:22 from TSA and 00:25 UT from VDA (see Section 4 and Table 2).

On the other hand, the shock's western flank approaches the IP field line connected to L1 only toward ∼01:45 UT. Depending on the assumed L1 solar-wind speed, the western shock flank lies within ≈0°–20° from the L1 footpoint between 01:45 and 02:30 UT. Note, however, that the shock1 fitting at these later times provides only a lower limit of the shock extension due to Thomson scattering effects. As the shock and sheath expand, the emission from the flanks originates farther from the sky plane and radial heliocentric distance. Hence, it becomes dimmer and harder to detect, causing an underestimate of the true shock extent. Since the TSA yields an L1 proton release time in the interval ≈01:54–02:18 UT and given its uncertainty, the proton release times are consistent with the shock's arrival at L1-connected field lines based on a high solar-wind speed of ∼500 km s^{-1}. However, the western flank of the shock remains far from the "expected" well-connected field lines for the observed wind speed of 370 km s^{-1} (∼54° longitude) even at the end of our shock-fitting sequence (03:30 UT).

In conclusion, we find that the eastern extension of the WL shock is consistent with the proton release at *STB*, while it seems that the particle release at L1 is associated with the western flank of the shock but requires a higher solar-wind speed than observed (assuming, of course, a Parker spiral). The extent of the WL shock's eastern flank fails to explain the SEP event observed at *STA* (TSA: 04:19–04:47 UT). The WL shock fittings at 03:30 UT show that the eastern flank is far away from the *STA*'s magnetically well-connected region (∼70°–80°). Finally, we find no evidence that CME2 played a role in the SEPs observed in L1 or *STA*. CME2 arrives too late at those magnetic field lines and has no obvious shock.

8. DATA-CONSTRAINED MODELING OF THE SHOCK IN THE HELIOSPHERE

We used the shock modeling of the previous section to constrain an MHD simulation of its IP propagation and evolution. The ENLIL code as implemented under NASA's Community Coordinated Modeling Center (see Odstrcil & Pizzo 2009) was used in this task. ENLIL is a 3D magnetohydrodynamic numerical model that simulates conditions pertinent to both a steady and a perturbed heliosphere from typically ∼0.1 to ∼1.7 au. It is important for the proper simulation of an IP shock to use proxies of the shock itself and not of its CME driver. For our simulation we applied a heliospheric disturbance, i.e., a hydrodynamic structure with enhanced density (thus pressure) and velocity in the inner simulation boundary. This disturbance was constrained by shock1's fitting central longitude and latitude, angular width (140°), and speed (2200 km s^{-1}) at the time when the shock reached 21.5 $R_{\odot}$ (0.1 au).

In Figure 11 we show three snapshots during the IP shock expansion from March 7 10:00 UT to March 8 15:00 UT. For each row in this figure, the three panels from left to right show the calculated plasma densities from different viewpoints: from the northern polar view of the ecliptic plane, in meridional plane view passing through Earth, and in the longitude–latitude map of a quasi-sphere at 1 au. The magnetic field lines connecting Earth (yellow circle), *STB* (blue circle), and *STA* (red circle) to the Sun (white circle) are shown as white dashed lines. The remaining symbols in Figure 11 correspond to the locations of other spacecraft and planets that are not relevant to this study. In this figure the IP shock can be traced as a curved, extended propagating compression front.

In Figure 12 we show the simulated values for the solar-wind speed (yellow line) and the corresponding in situ measurements (blue line); the time when the shock arrived at L1 is labeled with a double arrow. The simulated shock arrived at Earth at March 8 10:12 UT, which is in very good agreement with the arrival time determined from the in situ data at 10:41 UT. Moreover, the simulation seems to track the velocity jump due to the shock relatively well at L1. Shock1 seems sufficient by itself to capture several features of the observations at L1.

Despite the good agreement between model and observations at L1, there is a significant discrepancy concerning the shock's arrival time at *STB*. The simulated shock arrives on March 9 at ∼04:45, while the in situ measurements show an arrival time on March 8 ∼13:35 UT. From the in situ *STB* data it is evident that the shock is riding on the leading edge of a corotating high-speed stream, which is not present in the model. This could be the reason for the earlier-than-predicted arrival time.

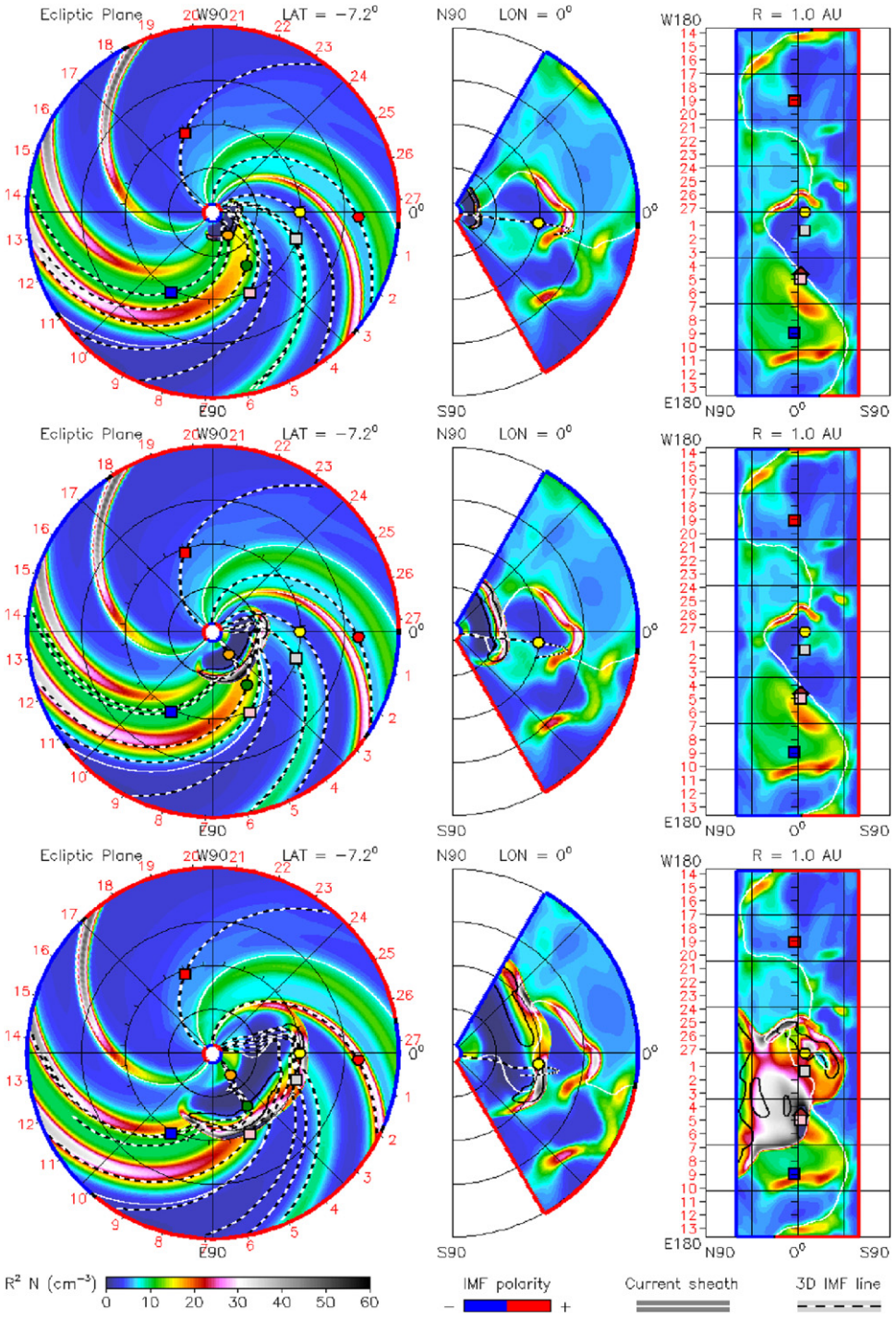

Figure 11. Simulation of first shock with ENLIL code from March 7–8 (top/middle panels: March 7 09:00/20:00 UT; bottom panel: March 8 15:00 UT). Left to right: the same snapshots at different projections. In each panel the color contours represent the simulated plasma density and the dashed black/white lines are the initial mass function (IMF) field lines that connect to different spacecraft (blue square for *STB* and red square for *STA*) and observing points (yellow circle for Earth).

(An animation of this figure is available.)

9. DISCUSSION AND CONCLUSIONS

Our study is a demonstration of the importance of shocks for tracing the generation and distribution of energetic particles. It also reveals the complexities in understanding the wide SEP longitudinal extents in the inner heliosphere.

Starting with the low corona connectivity, the proton release times, determined with the VDA and TSA techniques, were consistent with EUV-W1's arrival time at the *STB* footpoint. However, we did not find any evidence that either of the two EUV waves reached the L1 or *STA* footpoint. Moreover, the delay in proton release time for L1 and *STA*

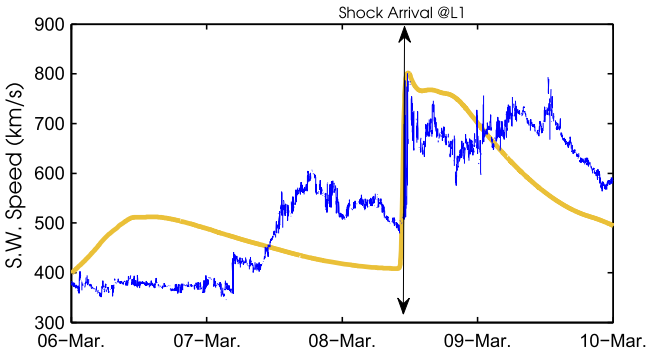

Figure 12. Simulated (yellow line) and in situ measurements (blue line) of the solar-wind speed at L1 from March 6 UT to March 10 UT. The double arrow marks the time when the shock arrived at L1.

could only be resolved by assuming that the energetic particles were released higher in the corona by the CME shock.

The 3D modeling of the CME shock allowed us to trace its lateral expansion higher in the corona and connect its longitudinal extent with the energetic proton release times. Clearly, the eastern (as seen from *STB*) flank of the shock was magnetically well connected with *STB*, consistent, within the uncertainties, with the proton release at *STB*. The shock's western flank reached within 10°–20° of the "expected" L1-connected field lines at the time of the energetic protons' release time. This angular separation may not be significant given the uncertainties of forward-modeling fittings in estimating the shock width (~8% of the total width or ~11° at 2:00 UT; Kwon et al. 2014). It is quite possible that a connection was established. Therefore, the delay in the proton release time at L1, relative to *STB*, can be attributed to the time it took the CME shock flank to reach the L1-connected magnetic field lines. Finally, the imaging analysis offers no convincing evidence that the shock was magnetically connected to *STA*. The proton release time at *STA* was significantly delayed compared to *STB* and L1, and the SEP event was weak. It is rather reasonable to expect that some transport process in the interplanetary medium allowed the energetic protons to reach *STA*.

However, the magnetic connectivity of any given point in the heliosphere is subject to considerable uncertainty during high-activity periods. For example, the previous multiple CME event of March 5 (Colaninno & Vourlidas 2015) may have significantly disrupted the IMF. Hence, the assumption that the IMF lines can be described by the simplistic Parker spiral model may not hold, and the longitude of the disrupted well-connected field lines may significantly differ from its nominal value. Our estimates of magnetic connectivity are based on simplistic magnetic configurations more representative of quite heliospheric conditions.

Regarding the energetic electrons, we found that the electron release times were associated with CME1 as well. The electron release at *STB* was slightly delayed (~5–10 minutes) compared to the protons. This delay is a frequent feature of SEP events (see Kouloumvakos et al. 2015) and can be attributed to selective acceleration or transport effects. At L1, the electron release was either simultaneous or delayed to the proton release, depending on the proton path length used in the TSA. At *STA*, the electron release time was almost 3 hr earlier than the protons. As we discussed above, it is highly unlikely that the shock is responsible. Even if a connection did eventually occur, it must be after ~04:00 UT. A careful inspection of all available data failed to uncover any other activity close to the *STA* footpoint. Therefore, we have to assume that the energetic electrons were not released directly onto the *STA*-connected field lines but were transported there. A weak anisotropy in the electron pitch-angle-dependent intensity distributions detected at *STA* (Dresing et al. 2014) favors this scenario.

In general, the longitudinal variation of SEP anisotropy is a crucial parameter for distinguishing between a moving particle source and a transport process, such as a cross-field diffusion. According to the anisotropy analysis by Dresing et al. (2014), our event was prompt and strongly anisotropic at *STB*, therefore favoring a shock origin relatively close to the Sun. At L1, the moderate anisotropy suggests that the SEPs are injected over a much wider angular range, consistent with a shock in the outer corona. At *STA*, the low anisotropy suggests that the SEPs reached that observing point through perpendicular diffusion. This is consistent with our results showing that the shock did not reach the *STA*-connected field lines. However, the electrons at *STA* tell a different story. Their short onset delay and rise time are inconsistent with perpendicular diffusion, which is a very slow process. A possible way to resolve this discrepancy is to assume that large-scale field line meandering (Laitinen et al. 2015) could contribute to cross-field transport and lead to a much faster access of particles to field lines at large cross-field distances.

In conclusion, we studied the relation between a major SEP event and two very energetic flare/CME events that occurred only 1 hr apart within the same AR. The eruptions were accompanied by shock phenomena throughout the corona and inner heliosphere manifested in various wavelengths (EUV, WL, radio). These events gave rise to an SEP event detected at locations (*STA STB*, and L1) spread over 120° from the source of the solar activity. Using multi-viewpoint EUV and WL remote sensing and in situ particle observations, we traced the sources of the proton release, and our key findings are as follows:

1. The SEP event at *STB*, L1, and likely *STA* was associated with CME1 from AR 11429.
2. The proton release time at *STB* is consistent with the arrival of both EUV-W1 and the shock1 eastern flank at the *STB* footpoint.
3. The particle release at L1 is broadly consistent with the timing and location of the western flank of WL shock1. We find no evidence that either of the EUV waves (EUV-W1 and EUV-W2) reached L1's well-connected region.
4. The SEP elemental abundance at *STB* and L1 is consistent with the average values observed in shock-related particle release processes and gradual SEP events.
5. Our 3D shock analysis cannot explain the particle release at *STA*. The weak anisotropies at *STA* suggest that IP cross-field diffusion may have been responsible for the transport of particles to *STA*.
6. The 3D geometrical fitting of the WL shock and the ENLIL simulation suggests an Earth-directed shock component that should not be confused with an Earth-directed CME.

Despite the comprehensive imaging and in situ observations across a wide swath of the inner heliosphere, the March 7 SEP

event proved to be a challenge. Specifically, the arrival of particles at *STA* located over 160° away from the flaring site is difficult to understand as it is inconsistent with our 3D shock analysis. We can offer two explanations. First, the 2012 March period was anything but quiet, and hence the magnetic connectivity in the heliosphere could be very different from a Parker spiral, as suggested by the short onset delay of the electrons at *STA*. Unfortunately, we do not have any way to know for sure. Second, it is likely that widespread SEP events may not be produced by a single mechanism, such as shock expansion. Transport processes may play a role, as suggested by the different anisotropies exhibited by the same event at the three locations. To make progress, therefore, we need denser in situ coverage across the inner heliosphere, especially closer to the Sun, where the injection and transport history can be more easily disentangled. The upcoming *Solar Orbiter* and *Solar Probe Plus* missions may shed new light on this problem.

We thank the anonymous referee for his/her valuable comments and suggestions, which led to significant improvement of the manuscript, and A. Papaioannou and Kuen Ko for useful discussions. The authors acknowledge support by European Union (European Social Fund—ESF) and Greek national funds through the "Operational Program Education and Lifelong Learning" of the National Strategic Reference Framework (NSRF)-Research Funding Program: "Thales. Investing in knowledge society through the European Social Fund." S.P. acknowledges support from an FP7 Marie Curie Grant (FP7-PEOPLE-2010-RG/268288). A.V. acknowledges support from NASA LWS under ROSES NNH10ZDA001N. Simulation results have been provided by the Community Coordinated Modeling Center at Goddard Space Flight Center through their public Runs on Request system (http://ccmc.gsfc.nasa.gov). The CCMC is a multi-agency partnership between NASA, AFMC, AFOSR, AFRL, AFWA, NOAA, NSF, and ONR. The ENLIL model was developed by D. Odstrcil at George Mason University/GSFC.

REFERENCES

Ajello, M., Albert, A., Allafort, A., et al. 2014, ApJ, 789, 20
Bougeret, J. L., Goetz, K., Kaiser, M. L., et al. 2008, SSRv, 136, 487
Cane, H. V., McGuire, R. E., & von Rosenvinge, T. T. 1986, ApJ, 301, 448
Cane, H. V., Mewaldt, R. A., Cohen, C. M. S., & von Rosenvinge, T. T. 2006, JGRA, 111, 6
Cane, H. V., Reames, D. V., & von Rosenvinge, T. T. 1988, JGR, 93, 9555
Cliver, E. W., Kahler, S. W., & Reames, D. V. 2004, ApJ, 605, 902
Colaninno, R. C., & Vourlidas, A. 2015, ApJ, 815, 70
Domingo, V., Fleck, B., & Poland, A. I. 1995, SSRv, 72, 81
Dresing, N., Gómez-Herrero, R., Heber, B., et al. 2014, A&A, 567, A27
Eyles, C. J., Harrison, R. A., Davis, C. J., et al. 2009, SoPh, 254, 387
Gómez-Herrero, R., Dresing, N., Klassen, A., et al. 2015, ApJ, 799, 55
Gopalswamy, N., Yashiro, S., Kaiser, M. L., Howard, R. A., & Bougeret, J.-L. 2001, ApJL, 548, L91
Guidice, D. A., Cliver, E. W., Barron, W. R., & Kahler, S. 1981, BAAS, 13, 553
Howard, R. A., Moses, J. D., Vourlidas, A., et al. 2008, SSRv, 136, 67
Huttunen-Heikinmaa, K., Valtonen, E., & Laitinen, T. 2005, A&A, 442, 673
Kaiser, M. L., Kucera, T. A., Davila, J. M., et al. 2008, SSRv, 136, 5
Kallenrode, M.-B., Wibberenz, G., Kunow, H., et al. 1993, SoPh, 147, 377
Klassen, A., Aurass, H., Klein, K.-L., Hofmann, A., & Mann, G. 1999, A&A, 343, 287
Kouloumvakos, A., Nindos, A., Valtonen, E., et al. 2015, A&A, 580, A80
Kouloumvakos, A., Patsourakos, S., Hillaris, A., et al. 2014, SoPh, 289, 2123
Krucker, S., Larson, D. E., Lin, R. P., & Thompson, B. J. 1999, ApJ, 519, 864
Kwon, R.-Y., Zhang, J., & Olmedo, O. 2014, ApJ, 794, 148
Laitinen, T., Kopp, A., Effenberger, F., Dalla, S., & Marsh, M. S. 2015, APJL, submitted (arXiv:1508.03164)
Lario, D., Ho, G. C., Roelof, E. C., Anderson, B. J., & Korth, H. 2013, JGRA, 118, 63
Lario, D., Raouafi, N. E., Kwon, R.-Y., et al. 2014, ApJ, 797, 8
Lemen, J. R., Title, A. M., Akin, D. J., et al. 2012, SoPh, 275, 17
Li, T., Zhang, J., Yang, S., & Liu, W. 2012, ApJ, 746, 13
Liu, Y. D., Luhmann, J. G., Lugaz, N., et al. 2013, ApJ, 769, 45
Magdalenić, J., Marqué, C., Krupar, V., et al. 2014, ApJ, 791, 115
Martínez Oliveros, J. C., Raftery, C. L., Bain, H. M., et al. 2012, ApJ, 748, 66
Mason, G. M., Gold, R. E., Krimigis, S. M., et al. 1998, SSRv, 86, 409
Mason, G. M., Korth, A., Walpole, P. H., et al. 2008, SSRv, 136, 257
Masson, S., Démoulin, P., Dasso, S., & Klein, K.-L. 2012, A&A, 538, A32
Mewaldt, R. A., Cohen, C. M. S., Cook, W. R., et al. 2008, SSRv, 136, 285
Miteva, R., Klein, K.-L., Kienreich, I., et al. 2014, SoPh, 289, 2601
Müller-Mellin, R., Kunow, H., Fleißner, V., et al. 1995, SoPh, 162, 483
Nitta, N. V., Liu, W., Gopalswamy, N., & Yashiro, S. 2014, SoPh, 289, 4589
Nitta, N. V., Schrijver, C. J., Title, A. M., & Liu, W. 2013, ApJ, 776, 58
Odstrcil, D., & Pizzo, V. J. 2009, SoPh, 259, 297
Ontiveros, V., & Vourlidas, A. 2009, ApJ, 693, 267
Page, E. S. 1954, Biometrika, 41, 100
Papaioannou, A., Malandraki, O. E., Dresing, N., et al. 2014, A&A, 569, A96
Park, J., Innes, D. E., Bucik, R., & Moon, Y.-J. 2013, ApJ, 779, 184
Patsourakos, S., Georgoulis, M. K., Vourlidas, A., et al. 2016, ApJ, 817, 14
Patsourakos, S., & Vourlidas, A. 2012, SoPh, 281, 187
Prise, A. J., Harra, L. K., Matthews, S. A., Long, D. M., & Aylward, A. D. 2014, SoPh, 289, 1731
Reames, D. V. 1999, SSRv, 90, 413
Reames, D. V. 2013, SSRv, 175, 53
Reames, D. V. 2014, SoPh, 289, 977
Reames, D. V., & Ng, C. K. 2004, ApJ, 610, 510
Richardson, I. G., von Rosenvinge, T. T., Cane, H. V., et al. 2014, SoPh, 289, 3059
Rouillard, A. P., Sheeley, N. R., Tylka, A., et al. 2012, ApJ, 752, 44
Sauer, H. H. 1993, ICRC, 3, 250
Schmidt, J. M., Cairns, I. H., & Lobzin, V. V. 2014, JGRA, 119, 6042
Stone, E. C., Cohen, C. M. S., Cook, W. R., et al. 1998, SSRv, 86, 357
Thernisien, A., Vourlidas, A., & Howard, R. A. 2009, SoPh, 256, 111
Torsti, J., Valtonen, E., Lumme, M., et al. 1995, in The SOHO Mission, ed. B. Fleck, V. Domingo, & A. Poland (Netherlands: Springer)
Vainio, R., Valtonen, E., Heber, B., et al. 2013, JSWSC, 3, A12
von Rosenvinge, T. T., Reames, D. V., Baker, R., et al. 2008, SSRv, 136, 391
Vourlidas, A., & Bemporad, A. 2012, in AIP Conf. Ser. 1436, Physics of the Heliosphere: A 10 Year Retrospective, ed. J. Heerikhuisen et al. (Melville, NY: AIP), 279
Vourlidas, A., Wu, S. T., Wang, A. H., Subramanian, P., & Howard, R. A. 2003, ApJ, 598, 1392
White, S. M., Benz, A. O., Christe, S., et al. 2011, SSRv, 159, 225
Wiedenbeck, M. E., Mason, G. M., Cohen, C. M. S., et al. 2013, ApJ, 762, 54
Wild, J. P. 1950, AuSRA, 3, 399
Yang, L., Zhang, J., Liu, W., Li, T., & Shen, Y. 2013, ApJ, 775, 39
Yashiro, S., Gopalswamy, N., Michalek, G., et al. 2004, JGRA, 109, 7105
York, D., Evensen, N. M., Martínez, M. L., & De Basabe Delgado, J. 2004, AmJPh, 72, 367
Zeitlin, C., Hassler, D. M., Cucinotta, F. A., et al. 2013, Sci, 340, 1080